RSC Advances

PAPER

View Article Online
View Journal | View Issue

Check for updates

Cite this: *RSC Adv.*, 2022, **12**, 16215

Sonochemical synthesis of inorganic cryogel $Ag_2Mo_3O_{10}$@Ag/AgO: structural characterization, antibacterial activity, and dye adsorption properties†

Adibeh Mohammadi, Akbar Mirzaei and Shahrzad Javanshir *

An additive-free ultrasonic-assisted synthesis of a multi-layered $Ag_2Mo_3O_{10}$@Ag/AgO cryogel (SMSSO) nanocomposite has been developed, and a possible formation mechanism of multi-layered SMSSO was proposed based on characterization results of scanning electron microscopy (SEM), energy-dispersive X-ray spectroscopy (EDX), X-ray diffraction (XRD), Raman spectroscopy, and diffuse reflection spectroscopy (DRS). The FE-SEM images demonstrated the formation process of the multi-layered SMSSO cryogel over time under sonication, starting with the growth of $Ag_2Mo_3O_{10}$ nanowires, and the formation of spherical nuclei which turn into an octahedron in the presence of excess silver ions. The antibacterial activity of the synthesized cryogel and its adsorption behavior for hazardous pollutant removal were explored. The results revealed that SMSSO exhibits excellent adsorption properties, with a maximum adsorption capacity of 277.77 mg g^{-1} and removal of 99/95% for 150 mg L^{-1} methylene blue (MB) by 0.005 g adsorbent doses at 60 °C and pH 9. It was also confirmed that the synthesized cryogels have good antibacterial activities against *Escherichia coli* (*E. coli*) and *Staphylococcus aureus* (*S. aureus*). The selective adsorption capability of the cryogel toward cationic dye molecules and antibacterial activity makes it a competent candidate for water purification.

Received 13th March 2022
Accepted 20th May 2022

DOI: 10.1039/d2ra01640k

rsc.li/rsc-advances

Open Access Article. Published on 30 May 2022. Downloaded on 12/31/2025 10:40:30 PM.
This article is licensed under a Creative Commons Attribution-NonCommercial 3.0 Unported Licence.

1. Introduction

Nowadays, water is considered to be a rare asset that must be protected. However, water pollution is becoming a universal scourge leading to environmental degradation, and reduced water quality poses a threat to public health. Furthermore, our environment suffers from the abundant amount of pollutants discarded by various industries, in particular organic dyes (methylene blue, neutral red, brilliant blue, *etc.*), heavy metals (Pb, Zn, Cd, Ni, *etc.*), and pathogenic bacteria that harm human health and the environment.[1,2]

So far numerous methods such as adsorption,[3–5] photocatalysis,[6] membrane filtration,[7,8] advanced oxidation[9,10] and antibacterial adsorbents[11,12] have been proposed to remove these pollutants. Among these methods, the adsorption techniques are especially attractive because of their high efficiency, simplicity of design, and ease of operation.[13] Many kinds of materials were designed as dye absorbents such as metal oxides,[14] carbon-based materials,[15] polymeric materials,[16] magnetic materials,[17] and cryogels.[18]

In recent years, various multi-component metal composites such as cobalt/selenium,[19] platinum/selenium,[20] silver/tungsten oxide,[21,22] molybdate/silver and their oxides[23,24] have been reported. Silver molybdenum oxides are one of the metal oxide-based dye adsorbents that have been synthesized over the past decades through various methods such as hydrothermal treatment,[25] coprecipitation,[26] and laser annealing[27] with different morphology. Hydrothermal is one of the most common methods in the synthesis of metal oxide nanoparticles. The greatest advantage of this method has been controlling the morphology of nanoparticles by changing time and temperature synthesis. Coprecipitation was another method used in the synthesis of molybdate silver oxide nanoparticles, which can be used to produce different types of molybdate silver oxide in different degrees of oxidation. For example, $Ag_2Mo_3O_{10}\cdot H_2O$ nanowires, showing high absorbing ability, were serendipitously synthesis from $AgNO_3$-assisted etching of ammonium phosphomolybdate.[26] However, only one study for the preparation of silver molybdates by the sonochemical method was reported.[28]

Although all of these methods have led to prominent results, the experimental condition contains low efficiency, high

Pharmaceutical and Heterocyclic Compounds Research Laboratory, Department of Chemistry, Iran University of Science and Technology, 16846-13114, Tehran, Iran. E-mail: shjavan@iust.ac.ir; Fax: +98-21-73227707; Tel: +98-21-77240346

† Electronic supplementary information (ESI) available: XRD pattern of $Ag_2Mo_2O_7/Ag_2MoO_4$, $Ag_2Mo_2O_7/Ag_2MoO_4$, and composite cryogel synthesized by ultrasound in H_2O/DMSO. Absorption spectra of different concentration of MB solution in the presence of SMSSO cryogel under dark conditions. See https://doi.org/10.1039/d2ra01640k

© 2022 The Author(s). Published by the Royal Society of Chemistry

Open Access Article. Published on 30 May 2022. Downloaded on 12/31/2025 10:40:30 PM.
This article is licensed under a Creative Commons Attribution-NonCommercial 3.0 Unported Licence.

temperature, and time of reaction, and the use of additives to control morphology makes them inefficient. Another property of metal oxides is their antibacterial activity, which can make them a good candidate for water purification.[29] A recent study has revealed the relationship between β-Ag_2MoO_4 crystals with different morphologies and unveiled the correlation between antibacterial activity, morphology, and surface energy. According to theoretical Wulff construction, morphologies with a larger (001) surface display better antibacterial properties which prove the effect of morphology on the antibacterial properties of metal oxide nanoparticles and help us in nanoparticles synthesis with high antibacterial properties through morphological formulation.[30] Another category of excellent dye absorbers is hydrogels which have received a lot of attention.[31,32] Hydrogels are typically super-porous networks formed by the solidification of soluble monomers or polymeric precursors at sub-zero temperatures and able to be very effective in removing and absorbing water pollutants through adsorption mechanisms like electrostatic, ion exchange, chemisorption, hydrogen-bonding, hydrophobic, complexation and interactions between target dyes and adsorbents. They are produced with a wide range of morphology and properties that can be designed for specific applications. These materials are heterophase, opaque, and porous with macro cavities.[33] Depending on the synthesis conditions such as the nature of the polymer monomer initiator, solvent and initiator and cross-linking, their concentration and ratios, temperature and freezing rate, the size of the macrospores can range from sub micrometers to 100 micrometers. Features such as high porosity, osmotic stability, mechanical strength, use of aqueous solvents, and facile synthesis, make them suitable for a variety of biological, biomedical, and water treatment applications.[34] Due to the extensive knowledge about adsorbents and their performance, *via* improving the adsorption capacity, simplifying the production method, and utilizing the synergistic properties of composite materials, adsorbents with higher efficiency can be prepared. Herein, an inorganic nanocomposite cryogel with specific morphology was fabricated by ultrasound waves at a short time and an environmental method. This composite cryogel showed good functional in removal methylene blue and high antibacterial. So, it can introduce as an efficient adsorbent for water purification (Scheme 1).

2. Experimental section

2.1. Materials and method

Silver nitrate ($AgNO_3$), ammonium heptamolybdate ($(NH_4)_6Mo_7O_{24}\cdot 4H_2O$) and methylene blue dye are purchased from Sigma-Aldrich, and used without further purification. Deionized water was produced by a Master-Q30 laboratory water purification system (Hi-tech Instruments Co., Ltd). A 20 kHz titanium probe of 5 mm diameter was used to generate ultrasonic waves (Top Sonic UPH-400, 20 kHz – 400 W, Ultrasonic Technology Development Co., Iran).[35,36] The *E. coli* (ATCC® 25922) and *S. aureus* (ATCC® 25923) were purchased from Iranian research organization for science and technology (IROST). FT-IR (Shimadzu 8400 S) and FE-SEM (Tescan Mira2) (D8 Advance Sol-X, Bruker Co., Germany) were used to study the structure and morphology of synthesized nanoparticles. The D8 advance X-ray diffractometer from Bruker revealed X-ray powder diffraction (XRD) patterns using Cu tube with a diffraction angle range of $2q = 10–75°$ while Tescan Mira3 displayed

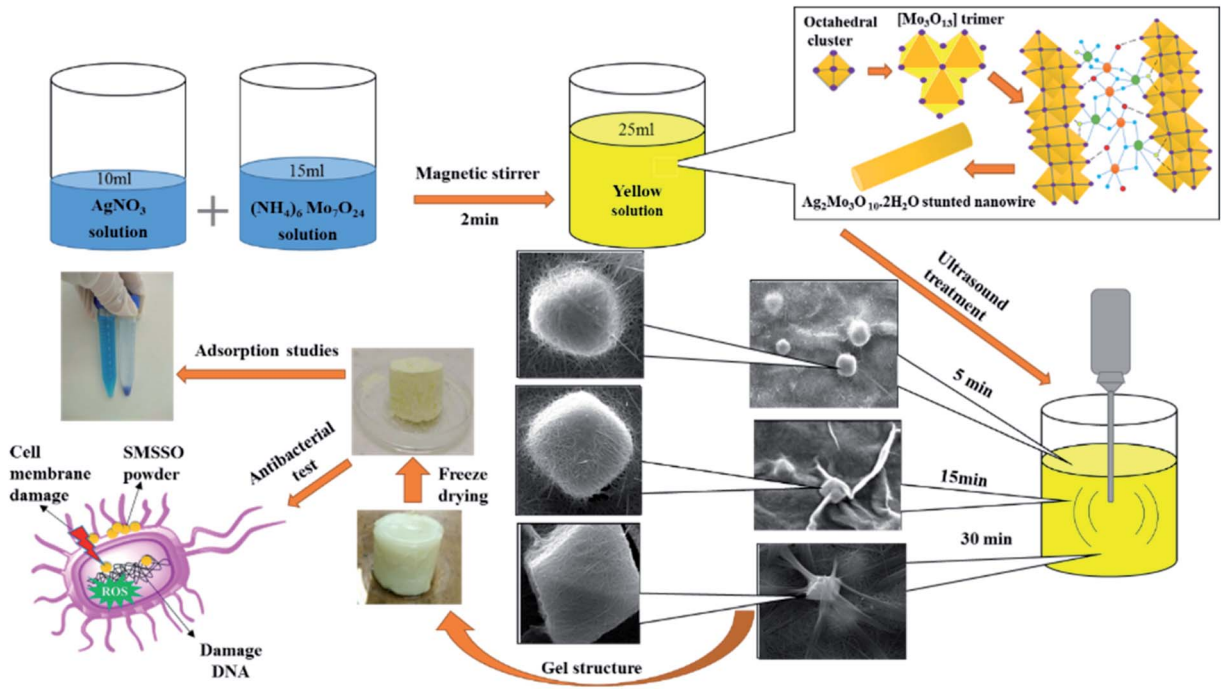

Scheme 1 Experimental steps of SMSSO composite cryogel formation.

© 2022 The Author(s). Published by the Royal Society of Chemistry

Open Access Article. Published on 30 May 2022. Downloaded on 12/31/2025 10:40:30 PM.
This article is licensed under a Creative Commons Attribution-NonCommercial 3.0 Unported Licence.

micrographs of samples. Also, Raman spectrum, and Zeta potential analysis was taken by TakRam N1-541, Teskan Co, Iran, and Malvern (zeta sizer model) instrument. The UV-Vis light absorption was studied using by UV-vis device of Shimadzu Corporation UV-2550.

2.2 Synthesis of cryogel based on $AgNO_3$ and $(NH_4)_6Mo_7O\cdot 4H_2O$

The cyrogels were synthesized by ultrasound-assisted precipitation method. The metal salts ($(NH_4)_6Mo_7O_{24})\cdot 4H_2O$ and $AgNO_3$ were dissolved in distilled water, and then mixed together with different Mo/Ag molar ratio (1 : 3, 1 : 2, 1 : 1, 2 : 1, and 3 : 1) and stirred for 2 min until obtaining a yellow solution. Specifically, 10 mL of $(NH_4)_6Mo_7O_{24}$ aqueous solution and 15 mL of aqueous solution of silver nitrate $AgNO_3$ with different Mo/Ag molar ratio were mixed and stirred for 5 min until obtaining a yellow solution. The mixture was then subjected to sonication by an ultrasonic probe (Iranian Ultrasonic Technology Company, 400 W, 20 kHz, 5 mm probe diameter) at nominal power of 60 W (real power delivered 4.16 W and power density 166.4 W L^{-1}) for different time (5 min, 15 min, and 30 min). The sonicator was turned on for 7 second and off for 3 second after keeping the probe 3 cm within the solution. The obtained hydrogels were freeze-dried for 24 h (−50 °C and 0.1 atm).

To study the effect of solvent and the radicals generated under ultrasonic irradiation on the formation of gel structure, the experiment was also performed in DMSO as effective hydroxyl radical scavenger, and under hydrothermal method at 120 °C temperature for appropriated time.

2.3 Adsorption experiments

Initially, MB solutions with concentrations ranging from 1 to 5 ppm were prepared. The calibration curve was obtained by plotting absorbance at the λ_{max} (663 nm) of MB and the absorption coefficient was determined. Solutions with concentrations ranging from 50, 100, 150, 200 ppm were prepared and 0.005 g of the adsorbent was added to 10 mL of each solution, and the adsorption capacities were measured. All steps were performed in complete darkness and the optimization of the factors affecting the adsorption process such as dye concentration, pH, temperature and the amount of adsorbent was performed.

2.4 Calculations

The removal efficiency (%) and adsorption capacity of $Ag_2Mo_3O_{10}$@Ag/AgO were determined according to the following equations:

$$\text{Efficiency } (\%) = \frac{C_0 - C_t}{C_0} \times 100 \quad (1)$$

$$q_t = \frac{(C_0 - C_t)V}{M} \quad (2)$$

where C_0 and C_t (mg L^{-1}) are the dye concentrations at the initial condition and time t, respectively; M (g) is the mass of adsorbent; V (L) is the volume of solution, and q_t (mg g^{-1}) is the amount of dye adsorbed onto composite cryogel $Ag_2Mo_3O_{10}$@-Ag/AgO at time t.

2.5 Antibacterial assay

Antibacterial activity evaluation of $Ag_2Mo_3O_{10}$@Ag/AgO cryogel was performed by the Kirby–Bauer disk diffusion susceptibility test protocol in Mueller–Hinton agar as a liquid culture medium. Briefly, a suspension of the bacteria strains (0.5×10^8 CFU mL^{-1}), *E. coli* or *S. aureus,* was spread on the culture medium. Then a filter paper disc of 1 cm in diameter was impregnated with a suspension of cryogels (0.030 mg mL^{-1}), placed in the Mueller–Hinton agar, and incubated at 37 °C for 24 hours.[37]

3. Results and discussion

3.1 Characterization

3.1.1 XRD pattern. The XRD patterns of synthesized cryogel with different Ag/Mo molar ratio were shown in Fig. 1a–c. The XRD pattern of sample with 1 : 1 Ag/Mo molar ratio (Fig. S1†) displayed the typical diffraction peaks of h-MoO_3/α-MoO_3/AgO composite with peaks at 2θ = 16.68, 19.76, 25.85, 29.52, 35.02,42.47, 43.36, 53.11, 56.33 correspond to the lattice planes [110], [200], [210], [300], [310], [224], [320], [420], [218] for hexagonal MoO_3 (h-MoO_3) and 2θ = 11.86, 23.20, 27.48, 29.68, 33.02, 34.70, 35.80, 38.52, 39.48, 42.47, 47.32 correspond to the lattice planes [020], [110], [021], [130], [101], [140], [041], [060], [150], [141], [210] for orthorhombic MoO_3 (α-MoO_3) Which matched the standard JCPDS no. 21-0569 and JCPDS no. 05-0508 cards, respectively. It emphasized the hexagonal and orthorhombic form of MoO_3.[38] The XRD pattern of composite cryogel with 2 : 1 Ag/Mo molar ratio was shown in Fig. 1a and displayed a pattern similar to Fig. 1b and c. Fig. 1b shows the X-ray diffractogram of composite cryogel with 3 : 1 Ag/Mo molar ratio. The square marked diffraction peaks at 2θ = 11.64, 16.25, 17.64, 23.06, 25.02, 27.13, 28.60, 29.72, 30.92, 31.91, 34.94, 47.89,49.84, were indexed as the orthorhombic $Ag_2Mo_3O_{10}\cdot 1.8H_2O$ corresponding to the lattice planes (101), (201), (210), (020), (311), (220), (221), (312), (203), (321), (501), (414), (432), respectively which is in good compliance with the standard (JCPDS no. 39-0045) card.[39] Also, studies proved the existence of the crystalline phase $Ag_2Mo_2O_7$ in the material. The existence of peaks in 28.56, 31.91, and 43.01 attributed to the lattice planes (020), (−121), (112), respectively (JCPDS no. 01-075-1505). In addition, the results showed different crystal phases of silver particles that are related to the (JCPDS no. 96-901-1609, 01-087-0719, 96-150-9-146) codes from a to c, respectively (Fig. 1a–c). Also, the peaks at 2θ values of 32.01, 36.97, and 55.91 correspond to the lattice planes (202), (220), and (141) are in good agreement with the standard JCPDS no. 01-084-1108 card[40,41] and confirmed the presence of AgO in the samples. The XRD pattern of composite cryogel with 4 : 1 Ag/Mo molar ratio (Fig. 1c) displayed a pattern similar to Fig. 1a and b. The XRD pattern of the powder obtained by hydrothermal method (see Fig. S2 in ESI†) revealed a combination of $Ag_2Mo_2O_7$/α-

Open Access Article. Published on 30 May 2022. Downloaded on 12/31/2025 10:40:30 PM.
This article is licensed under a Creative Commons Attribution-NonCommercial 3.0 Unported Licence.

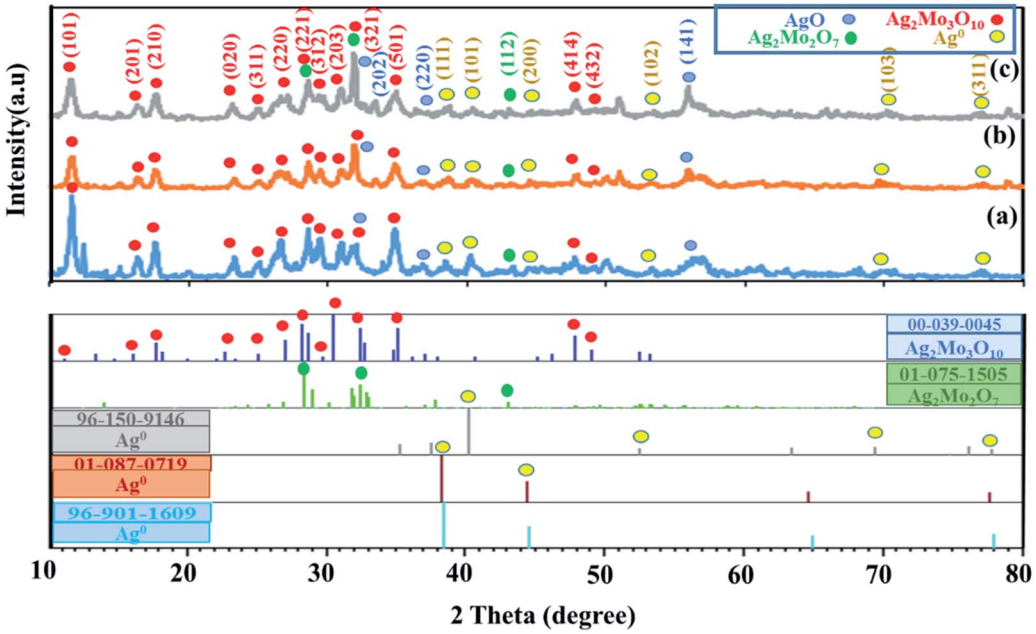

Fig. 1 XRD pattern of synthesized cryogels with different Ag/Mo molar ratio (a) 2 : 1, (b) 3 : 1, and (c) 4 : 1.

$Ag2MoO_4$. The lattice planes (111), (021), (020), (122), (112), (220), (200), (132), (112), and (300) are due to diffraction peaks at (24.61), (26.93), (28.44), (31.20), (32.76), (33.88), (34.99), (48.01), (34.01), (42.02), (49.78) for $Ag_2Mo_2O_7$ (JCPDS no. 01-075-1505) and the lattice planes (220), (311), (222), (400), (422), (511) are attributed to diffraction peaks (27.46), (31.20), (33.88), (48.01), (47.92), (49.78) for α-Ag_2MoO_4, respectively (JCPDS card no. 00-008-0473). The XRD pattern in Fig. 1b indicates three peaks at 41.7, 43.1 and 60.9 corresponding to the $Ag_2Mo_2O_7$ (JCPDS card no. 01-075-1505). Also, the XRD pattern of black powder which was synthesized by ultrasonication in DMSO displayed a two-phase mixture of $Ag_2Mo_2O_7/Ag_2MoO_4$ wight reference code (JCPDS no. 01-075-1505) and (JCPDS no. 01-075-0250), respectively (Fig. S3†). In addition, the XRD pattern of cryogel synthesized by ultrasound in DMSO–H_2O mixtures proved the formation of $Ag_2MoO_4/Ag_2Mo_2O_7/Ag$ with reference code (JCPDS no. 00-021-1340), (JCPDS no. 01-075-1505) and (JCPDS no. 04-0783), respectively (Fig. S4†). This proved that the gel structure didn't form in the absence of water.

3.1.2 Morphology. Fig. 2 shows the FESEM for the synthesized SMSSO composite cryogel with 3 : 1 Ag/Mo molar ratio for varying time periods of sonication *i.e.*, 5, 15, and 30 min. When the two colorless solutions of $AgNO_3$ and $(NH_4)_6Mo_7O_{24}$ were mixed, a light-yellow color appears corresponding to the short and thin wires of silver molybdate oxide. Ultrasonic treatment was applied immediately after the solution turned light yellow. FESEM images show that short nanowires were changed to long nanowire with an average diameter of 50 nm after 5 min sonication which intertwined and tangled to form spherical nodes (Fig. $2a_{1-4}$). These spherical nodes were transformed into cubic nuclei as the ultrasound treatment continues. FESEM images clearly revealed that by prolonging the sonication time to 15 min the short silver molybdate nanowires were converted to long and thin nanowires reaching over a few hundred microns in length. Completed growth process by Ostwald ripening and oriented attachment provoke ultra-long nanowires formation[26]. With increasing sonication time, the spherical nodes were transformed into cubic nodes of $Ag_2Mo_3O_{10}$ (Fig. $2b_{1-4}$). An extended sonication time of 30 min results in the formation of ultra-long wires and their entanglement causes the formation of the octahedral knots (Fig. $2c_{1-4}$) (Fig. 4b). According to research conducted by Chaodong He and *et al.*, hydrogen and hydroxyl radicals ($H^{\bullet}$, $OH^{\bullet}$) are formed by the decomposition of water during ultrasonic irradiation and silver ions in solution can receive electrons from $H^{\bullet}$ and convert Ag^+ to silver (Ag^0) nanoparticles.[42] On the other hand, AgO could be formed by oxidation of Ag^+ by H_2O_2 produced by cavitation during ultrasonic irradiation.

In fact, during the ultrasonic treatment, the excess Ag^+ in the solution is reduced to Ag^0 nanoparticles by $H^{\bullet}$ radicals generated during cavitation and placed as on the surface of silver molybdate nanowires (Fig. $2b_4$). When the experiment was performed in DMSO, no gel formed and a black powder was obtained and characterized as a mixture of $Ag_2Mo_2O_7/Ag_2MoO_4$ (Fig. 5a and S2†), however gelation occurred in the mixture H_2O/DMSO and according to the XRD pattern a mixture of $Ag_2Mo_2O_7/Ag_2MoO_4/Ag$ was formed (Fig. 5d and S3†). In H_2O/DMSO mixture, DMSO acted as hydroxyl radical scavenger, so AgO did not form and the H reduced silver ions to Ag^0. The experiment was also performed under hydrothermal conditions, in which a dark brown powder was obtained and characterized as a mixture of $Ag_2MoO_4/Ag_2Mo_2O_7$ without any gelling process (Fig. 5b and S1†). This proves that the growth of short nanowires is only completed in the presence of silver nanoparticles and under sonication, forming a porous gel structure by creating very long and entangled nanowires.

© 2022 The Author(s). Published by the Royal Society of Chemistry

Open Access Article. Published on 30 May 2022. Downloaded on 12/31/2025 10:40:30 PM.
This article is licensed under a Creative Commons Attribution-NonCommercial 3.0 Unported Licence.

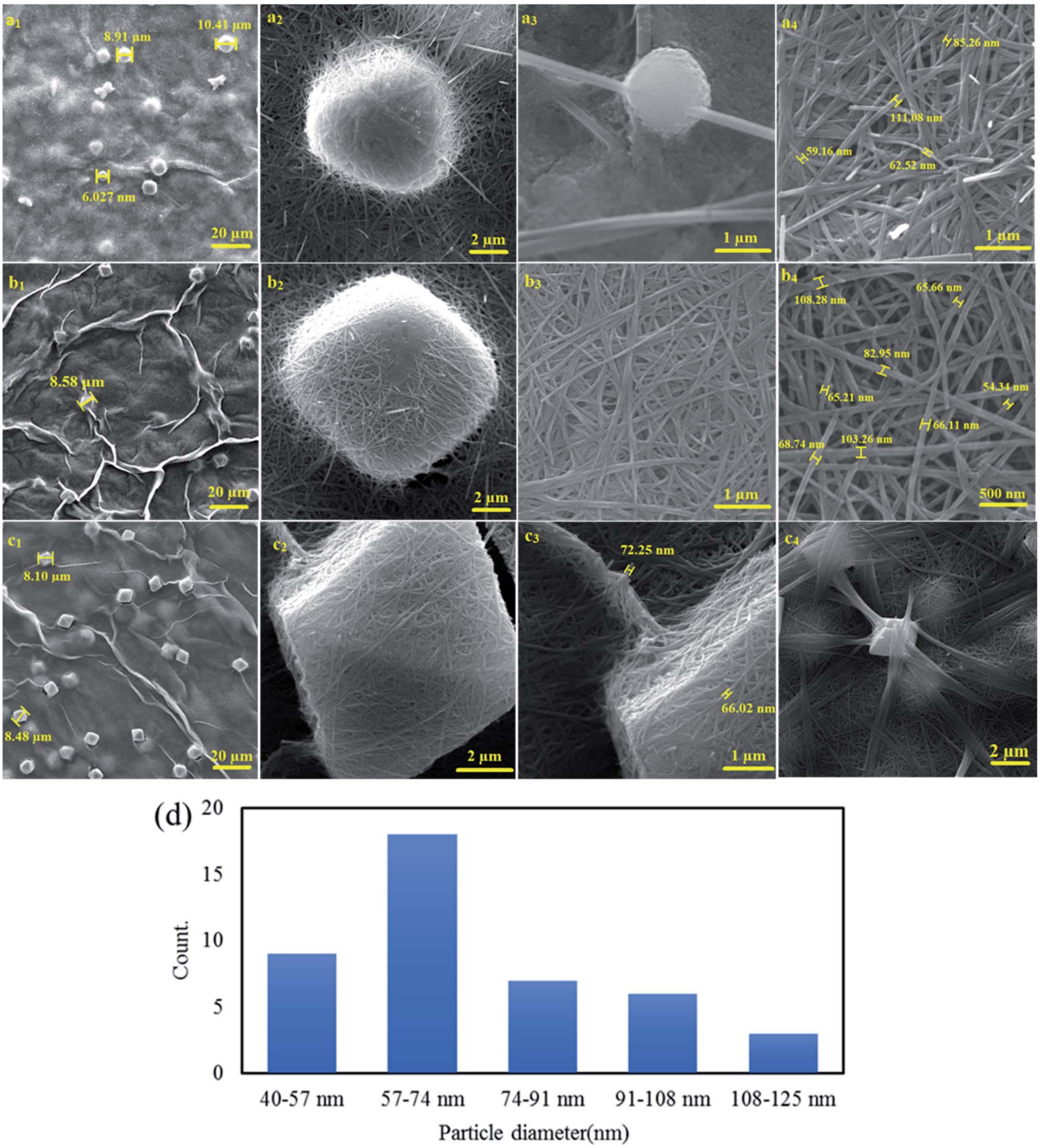

Fig. 2 FE-SEM micrographs of SMSSO composite cryogel with 3 : 1 Ag/Mo molar ratio ($Ag_2Mo_3O_{10}$@Ag/AgO) after 5 min (a_{1-4}), 15 min (b_{1-4}), 30 min sonication (c_{1-4}) and the particle size histogram of $Ag_2Mo_3O_{10}$ nanowires (d).

The particle size of molybdate silver oxide nanowires, as shown in Fig. $2b_4$, was plotted (Fig. 2d). The particle size scatter was determined between 40–125 nm and most nanowires had a particle size between 57–74 nm. FESEM micrographs of composite prepared with 1 : 2 Ag/Mo molar ratio are shown in Fig. $3a_{1-3}$. The formation of uniform straw-like nanowires morphology can be clearly observed at different magnification. It is clearly observed that when the molybdate ions were in excess, no knots formed on the surface of the short and thin nanowires even after a prolonged sonication time. The FE-SEM micrographs for nanocomposite with 2 : 1 Ag/Mo molar ratio were displayed in Fig. $3b_{1-3}$. Uniform long nanowires are

© 2022 The Author(s). Published by the Royal Society of Chemistry

Open Access Article. Published on 30 May 2022. Downloaded on 12/31/2025 10:40:30 PM.
This article is licensed under a Creative Commons Attribution-NonCommercial 3.0 Unported Licence.

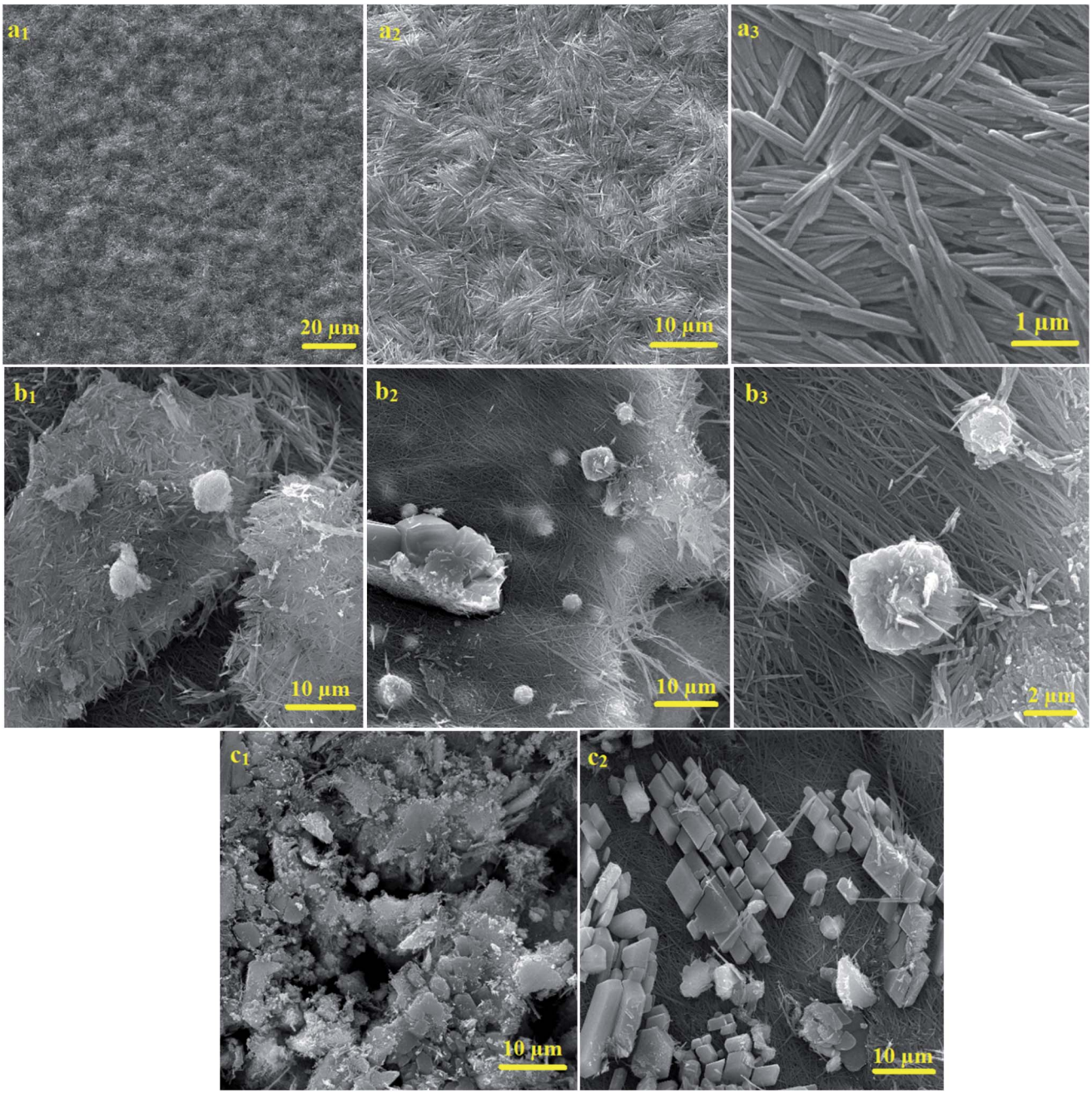

Fig. 3 FE-SEM micrographs of 2 : 1 ratio of $Ag_2Mo_3O_{10}$ with excess amount of $(NH_4)_6Mo_7O_{24}$ (a_{1-3}), FE-SEM micrographs of sample 2 : 1 ratio of SMSSO with excess amount of $AgNO_3$ (b_{1-3}). FE-SEM micrographs of sample 1 : 1 molar Ag/Mo ratio SMSSO ($c_{1,\ 2}$).

formed and nucleation has taken place, but the formation of nanowire sheets remains incomplete. So, the gel structure is more fragile than the 3 : 1 sample. In some areas, it has been observed that due to the non-optimal ratio of silver nitrate to ammonium heptamolybdate, the growth process of the nanowire is not completed and they are short and stuck together. The FE-SEM images of the synthesized gel with 1 : 1 molar ratio shows that when the amount of silver ions in the reaction solution does not reach a certain limit, a regular and cohesive structure is not seen. As you can see in the Fig. $3c_{1,\ 2}$, part of the structure is mass-like and amorphous, no nucleation has taken place and no intertwined strands have formed. In another part of the structure, very long and intertwined filaments are seen, which shows that some filaments have completed their growth. The apparent structure of the material also showed that in this case, the gel formed was very loose and did not have structural cohesion. Furthermore, the physical and mechanical properties of the synthesized hydrogel were investigated and it was shown that it has very low weight and very high structural strength. Its density was measured at about 0.03 g cm^{-3} (Fig. 4a).

3.1.3 FT-IR and Raman spectra. The FT-IR spectra of $Ag_2Mo_3O_{10}$@Ag/AgO was illustrated in Fig. 6a. The vibrational band

© 2022 The Author(s). Published by the Royal Society of Chemistry

Open Access Article. Published on 30 May 2022. Downloaded on 12/31/2025 10:40:30 PM.
This article is licensed under a Creative Commons Attribution-NonCommercial 3.0 Unported Licence.

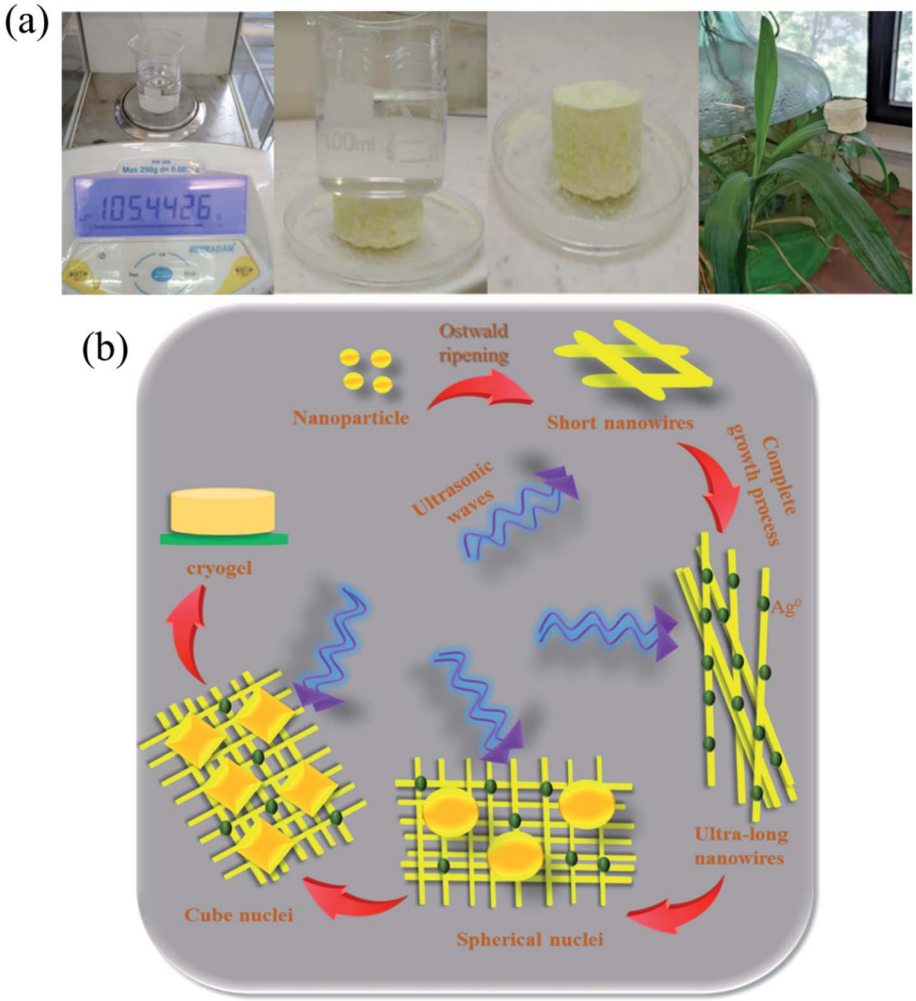

Fig. 4 The strength and lightness of the cryogel were evaluated (a) and proposed mechanism of cryogel formation under sonication (b).

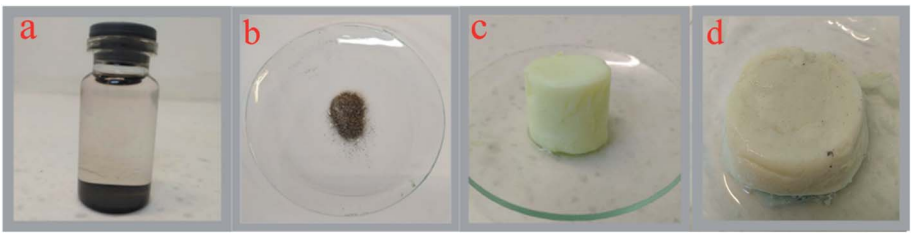

Fig. 5 (a) $Ag_2Mo_2O_7/Ag_2MoO_4$ synthesized in DMSO by ultrasonication (b) $Ag_2Mo_2O_7/Ag_2MoO_4$ synthesized by hydrothermal method (c) $Ag_2Mo_3O_{10}$@Ag/Ag_2O cryogel in H_2O under sonication waves (d) $Ag_2Mo_2O_7/Ag_2MoO_4$/Ag cryogel in H_2O/DMSO under sonication.

appeared at 651 cm^{-1} was attributed to Ag–OMo which may cause doped of Ag nanoparticles over $Ag_2Mo_3O_{10}$ nanowires. The bands appearing at 501 cm^{-1} and 566 cm^{-1} are related to the stretching vibration of Mo–O in MoO_3. The vibrational peaks observed at 887 and 944 cm^{-1} are related to Mo=O stretching vibrations.[26,43] The absorbance peak at 431 cm^{-1} was assigned to Ag–O stretch.[44] The broad absorption bands in 3000 cm^{-1} to 3500 cm^{-1} region and 1403 cm^{-1} correspond to the stretching and the bending vibrations of hydrogen bonded –OH group of water molecules. Raman spectra of $Ag_2Mo_3O_{10}$@Ag/AgO was displayed in Fig. 6b. The characteristic peaks of $Ag_2Mo_3O_{10}$ and AgO were present and matched well with similar reference Raman spectra.[45,46] The bands observed at 194, 219, 372, 591, 760 and 872 cm^{-1} correspond to bridging Mo–O–Ag, bending vibration of O–Mo–O, asymmetric and symmetric stretching vibrations of O–Mo–O respectively. The peak observed at 947 cm^{-1} was attributed to Mo–O symmetric stretching.

© 2022 The Author(s). Published by the Royal Society of Chemistry

Open Access Article. Published on 30 May 2022. Downloaded on 12/31/2025 10:40:30 PM.
This article is licensed under a Creative Commons Attribution-NonCommercial 3.0 Unported Licence.

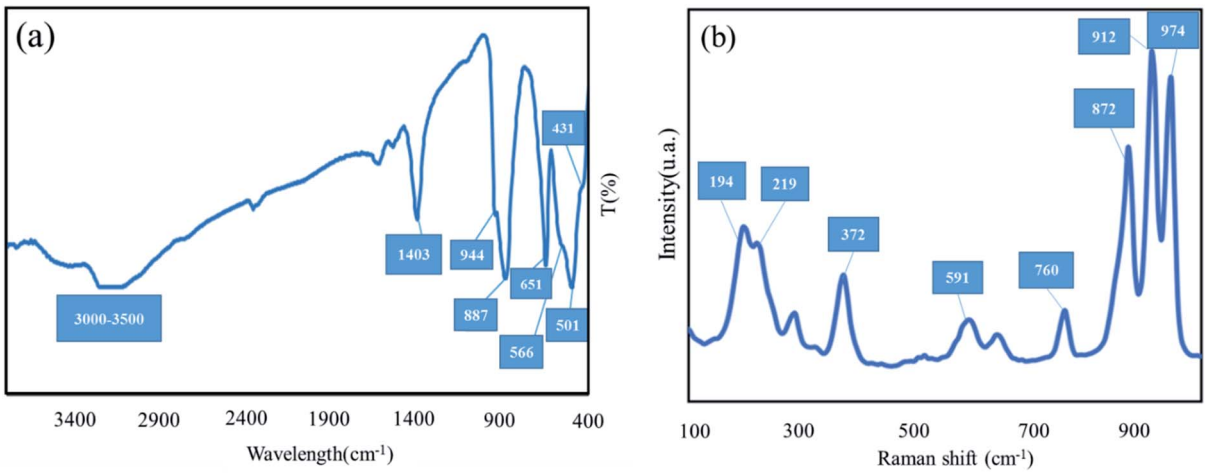

Fig. 6 FT-IR spectra (a) and Raman spectroscopy of SMSSO nanocomposite cryogel at $\lambda = 532$ nm (b).

3.1.4 Zeta potential and differential reflectance spectroscopy analysis. Zeta potential measurements were highly consistent with particle size distribution data and showed suspension stability. The magnitude of the zeta potential indicates the magnitude of the stability of the suspension. If all particles in the suspension have very positive or very negative zeta potential, they repel strongly and will not tend to stick together in solution so they will form a very stable suspension. The zeta potential of the synthesized cryogel composite was −59.5 mV. Particles with very positive or very negative zeta potentials have high stability in the colloidal medium (Fig. 7a). DRS analysis was performed to investigate the optical properties and energy of the gap band. The energy bands were determined by Kubelka–Munk theory using the eqn (3):

$$(\alpha, h, \nu)^2 = h\nu - E_g,\ \alpha = -1/t \ln T \quad (3)$$

where A, h, α, ν, T, t, and E_g imply the absorbance, Planck constant, absorption coefficient, frequency, transmittance, thickness, and energy gap. It can be seen that the band gaps of the nanoparticle, silver oxide and silver molybdate oxide were merged. Finally loading silver nanoparticle and silver oxide lead to reduced bandwidth (Fig. 7b).[45]

3.1.5 Energy-dispersive X-ray spectroscopy. EDX analysis was used to identify the elements present in the as-prepared SMSSO composite cryogel ($Ag_2Mo_3O_{10}$@Ag/AgO) and the result is presented in Fig. 8. The result discloses the presence of O, Mo, and Ag elements in the material without any other significant impurities. According to the measurements, the signals attributed the oxygen, molybdenum, and silver an atomic weight percentage of 10.31, 55.83, and 33.85% respectively.

3.2 Adsorption studies

3.2.1 Concentration optimization. MB was chosen as the model pollutant and a 200 mg L^{-1} of MB stock solution was prepared for the following adsorption experiments. To achieve the best adsorption concentration for the synthesized

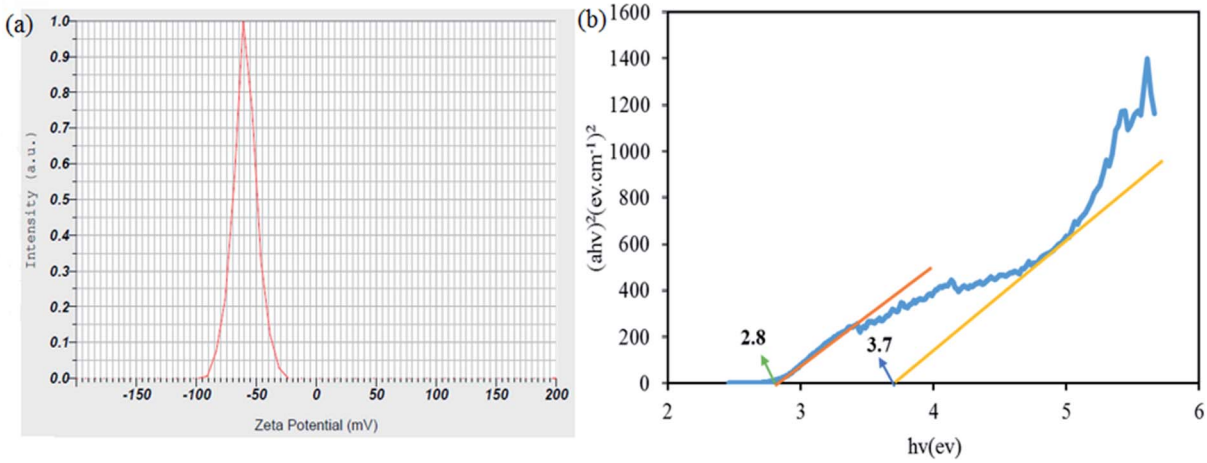

Fig. 7 Zeta potential (a) and (b) energy band gaps of SMSSO composite cryogel.

© 2022 The Author(s). Published by the Royal Society of Chemistry

Open Access Article. Published on 30 May 2022. Downloaded on 12/31/2025 10:40:30 PM.
This article is licensed under a Creative Commons Attribution-NonCommercial 3.0 Unported Licence.

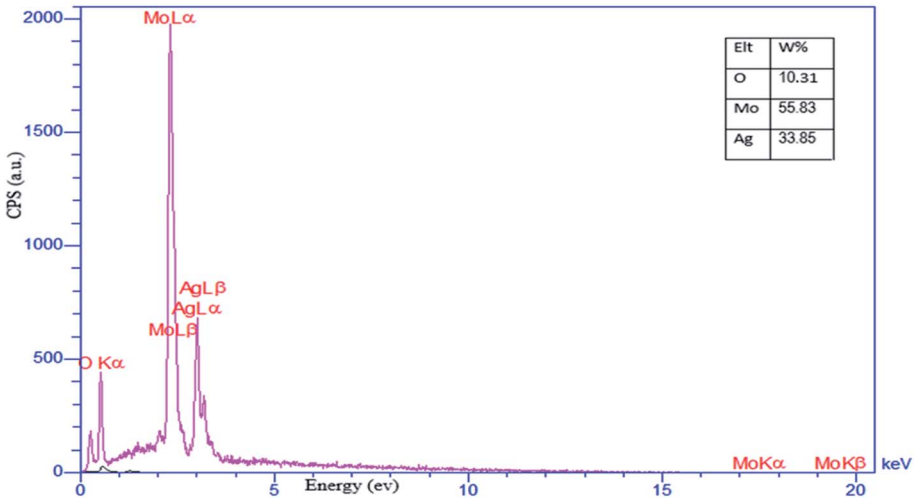

Fig. 8 EDX analysis of nanocomposite cryogel SMSSO.

composite cryogel, we created different concentrations of methylene blue, and the adsorption capacity of all of them was calculated and analyzed. Here, 0.5 g L^{-1} of the adsorbent dose was used (Fig. 9a and S5†). The combination of molybdate silver oxide with silver nanoparticles has resulted in more adsorption sites being provided to the raw material through OH groups and empty silver orbitals.

3.2.2 Effect of pH. The solution pH is an important parameter that affects the adsorption of dye molecules as it can affect the capacity of adsorption of the adsorbent.[47] Fig. 9b was showed the adsorption capacity of hydrogel composite of

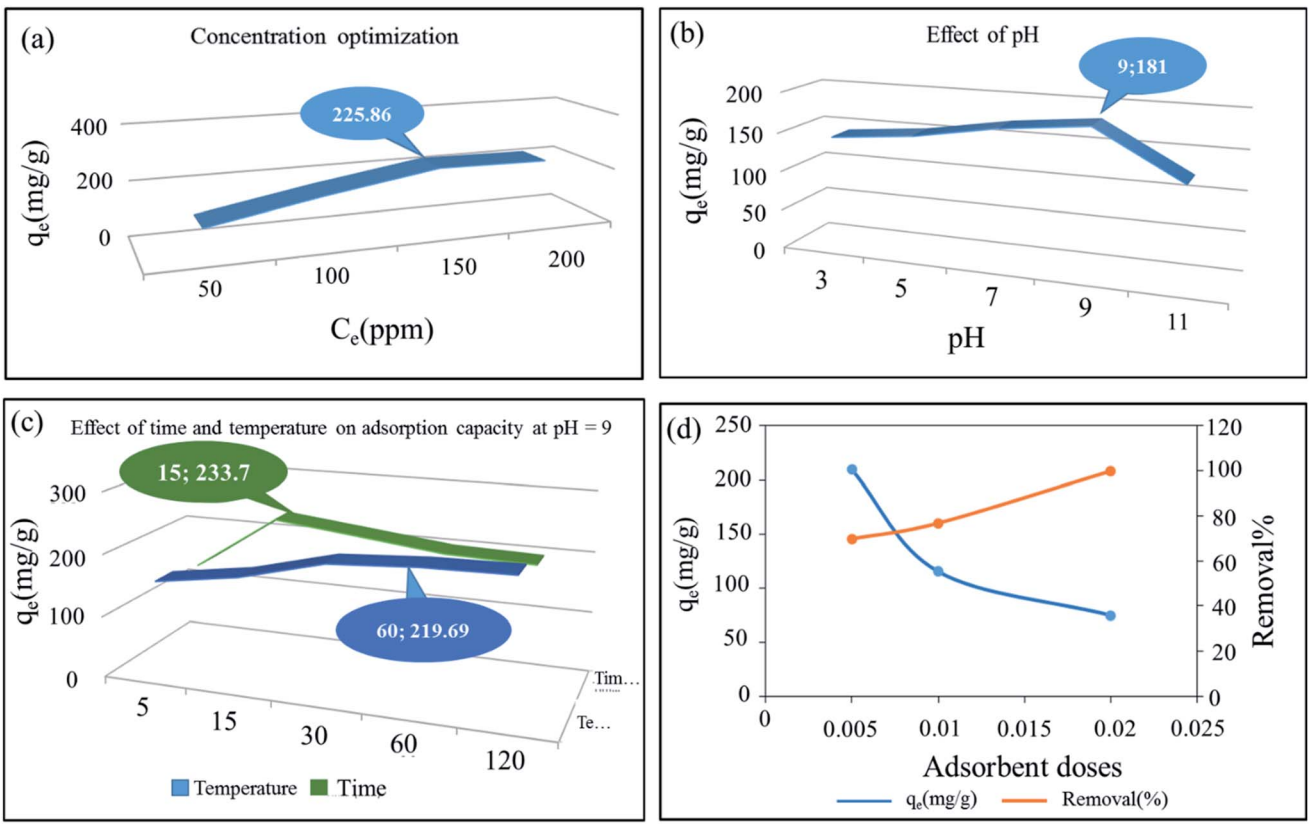

Fig. 9 Nonlinear plots of adsorption isotherms of SMSSO cryogel composite. Effect of (a) concentration (b) pH (c) time and temperature (C_0 = 150 ppm, adsorbent dose = 0.005 g), and (d) adsorbent dose on adsorption capacity of SMSSO.

© 2022 The Author(s). Published by the Royal Society of Chemistry

Open Access Article. Published on 30 May 2022. Downloaded on 12/31/2025 10:40:30 PM. This article is licensed under a Creative Commons Attribution-NonCommercial 3.0 Unported Licence.

$Ag_2Mo_3O_{10}$@Ag/AgO by changes pH from 3 to 11. Experiments showed that with increasing the pH from 3 to 9 the adsorption capacity increased but with increasing the pH up to 11 the adsorption capacity decreased significantly. The increase in pH value of the reaction container suggests that a great deal of OH ions are present and in fact, the adsorbent surface is negatively charged. The electrostatic force created between the negative adsorbent surface and the positive surface of methylene blue increases the adsorption capacity. Besides, silver nanoparticles can receive negative OH groups at their surface through their empty sites. The decrease in adsorption capacity from pH 9–11 can be attributed to the repulsion of the catalyst surface and methylene blue due to the formation of positive sites, which may be due to the hydrolysis of the adsorbent surface.[26] Also, we suggest that at pH > 9, the amount of OH^- ions in the environment increases to such an extent that there is competition between these ions and the adsorbent, which ultimately reduces the adsorption capacity.[48]

3.2.3 Adsorbent dose effect. Studies showed that the adsorption capacity and removal percentage are inversely related to each other, by adding more adsorbents, more contaminants are removed, but because the active sites on the adsorbent are filled quickly by contaminants, adsorption capacity is reduced by adding more adsorbent.[49] The experimental results revealed that by applying optimal operating conditions, the synthesized $Ag_2Mo_3O_{10}$@Ag/AgO had the highest adsorption capacity for the absorbent dose of 0.005 g, but for the adsorbent dose of 0.02 g, highest removal percentage of 99.956% is reached. Therefore, for all further experiments adsorbent dose was fixed at 0.005 g (Fig. 9d).

3.2.4 Effect of time on adsorption capacity. The experimental data showed that the increase in the adsorption time from 5 to 15 min, is accompanied by an increase in adsorption capacity reaching its maximum value, then by prolonging the time to 30 min a downward trend and finally stabilization is observed. This indicates that the adsorbent has filled most of its adsorption sites within the first 15 min and has reached its maximum absorption (Fig. 9c).

3.2.5 Effect of temperature on adsorption capacity. The effect of temperature was investigated for optimal adsorbent dose 0.005, concentration 150 ppm, time 15 min, and pH 9 at temperatures of 20, 40, 60, 80, and 100 °C. The absorbent capacity has increased from 20 to 60 °C but from 60 to 100 °C this increase continues with a very gentle slope and becomes constant. As a result, 60 °C was selected as the optimum temperature. The rise in removal efficiency with the increase in temperature indicated that the adsorption process is endothermic (Fig. 9c).

The adsorption capacity of the synthesized cryogel under optimal condition (10 mL of $C_0 = 150$ ppm, pH = 9, 0.005 g and 60 °C) in comparison with $Ag_2Mo_3O_4$ nanowires under optimal conditions (500 mL of 2×10^{-5} M, pH = 7, 0.020 g and 25 °C) showed that the gelling and the creation of new morphology increase the adsorption capacity from 175 for $Ag_2Mo_3O_{10}$ nanowires to 277.77 for the synthesis cryogel. Different thermodynamic parameters were computed to scrutiny the nature of adsorption. These parameters contain change in enthalpy (ΔH°), entropy (ΔS°), and Gibb's free energy change (ΔG°), and quantities were obtained *via* experiments at several temperatures. Calculations were performed by following Van't Hoff equations:

$$\Delta G^\circ = -RT \ln K \tag{4}$$

$$\ln K_c = -\frac{\Delta G}{RT} = -\frac{\Delta H}{RT} + \frac{\Delta S}{R} \tag{5}$$

$$K_c = \frac{q_e}{C_e} \tag{6}$$

where R is the gas constant with quantity 8.314 J mol^{-1} K^{-1}. K_c (L g^{-1}) displays the distribution coefficient, q_e (mg g^{-1}) is the value of dye adsorbed at equilibrium per gram of adsorbent, T (K) is the temperature of absolute, Ce (mg L^{-1}) illustrates the equilibrium concentration of dye in aqueous solution. For the assessment of values of ΔS° and ΔH°, a Van't Hoff graph of $\ln K$ *vs.* $1/T$ was designed (Fig. S6†) and measured from the slope and intercept. Gibbs free energy change (ΔG°) was calculated using the following equation:

$$\Delta G^\circ = \Delta H^\circ - T\Delta S^\circ \tag{7}$$

Table 1 exhibits the calculated thermodynamics properties for prepared adsorbent. The quantity of ΔH° is positive which shows the endothermic nature of adsorption. The negative amount of ΔG° for all temperatures indicates the spontaneous adsorption of methylene blue on the SMSSO adsorbent. The value of ΔG° decreases with increasing temperature, which indicates an increase in adsorption at higher temperatures. Also, the positive ΔS° gives increased randomness on solid–

Table 1 Thermodynamic parameters for methylene blue adsorption onto SMSSO cryogel

	Thermodynamics parameters				
Adsorbent	T (K)	K_c (L g^{-1})	ΔG° (kJ mol^{-1})	ΔH° (kJ mol^{-1})	ΔS° (J mol^{-1} K^{-1})
SMSSO cryogel	293.15	2.10	−14085.35	12.23	48.09
	313.15	2.79	−15047.15		
	333.15	4.74	−16008.95		
	353.15	5.47	−16970.75		
	373.15	5.75	−17932.55		

© 2022 The Author(s). Published by the Royal Society of Chemistry

Open Access Article. Published on 30 May 2022. Downloaded on 12/31/2025 10:40:30 PM.
This article is licensed under a Creative Commons Attribution-NonCommercial 3.0 Unported Licence.

Table 2 Comparison of data of two isotherm models for MB adsorption

	Langmuir isotherm			Freundlich isotherm		
Material	b (L mg^{-1})	q_m (mg g^{-1})	R^2	K_F ((mg^{-1} Ln) g^{-1})		R^2
SMSSO cryogel	10.19	277.77	0.9956	10.68	2.56	0.8875

Table 3 Adsorption kinetic parameters of MB adsorption

	Pseudo-first-order model		Pseudo-second-order model	
Material	K_1 (min^{-1})	R^2	K_2 (g mg^{-1}.min)	R^2
SMSSO cryogel	0.199	0.9865	0.068	0.9986

liquid interface.[50] All thermodynamic parameters are shown in Table 3.

3.2.6 Adsorption isotherm studies. Adsorption isotherms were used to investigate the relationship between the amount of adsorbed MB onto the SMSSO surface and the concentration of MB in the aqueous phase at equilibrium state. Non-linear equilibrium models of Langmuir, Freundlich, and Temkin were utilized to fit the experimental data. The linear equations of the equilibrium models Langmuir, Freundlich, and Temkin are present in eqn (8)–(10).

$$\frac{1}{q_e} = \frac{1}{q_{max}} + \frac{1}{C_e q_{max}} b \quad (8)$$

$$\ln q_e = \ln k_f + \left(\frac{1}{n}\right) \ln C_e \quad (9)$$

$$q_e = \frac{RT}{b} \ln C_e + \frac{RT}{b} \ln K_T \quad (10)$$

where q_e (mg g^{-1}) is the amount of MB dye adsorbed at equilibrium, q_{max} (mg g^{-1}) is the maximum adsorption capacity, and C_e (mg L^{-1}) is the concentration of MB dye at equilibrium. K_f, is the Freundlich constant, n is the dimensionless constant indicating the adsorption intensity. K_T (mg L^{-1}) is Temkin constant, R (8.314 J.mol K^{-1}) is the universal gas constant, T (K) is temperature and b (J mol^{-1}) is the heat of adsorption. Considering the values of R^2 values (Table 2 and Fig. 10a and b) obtained from the isotherm models, it can be concluded that the adsorption process of MB dye on the surface of synthesized cryogel has a high compliance with Langmuir isotherm models (R^2 = 0.9956). Moreover, this result also indicates that the MB

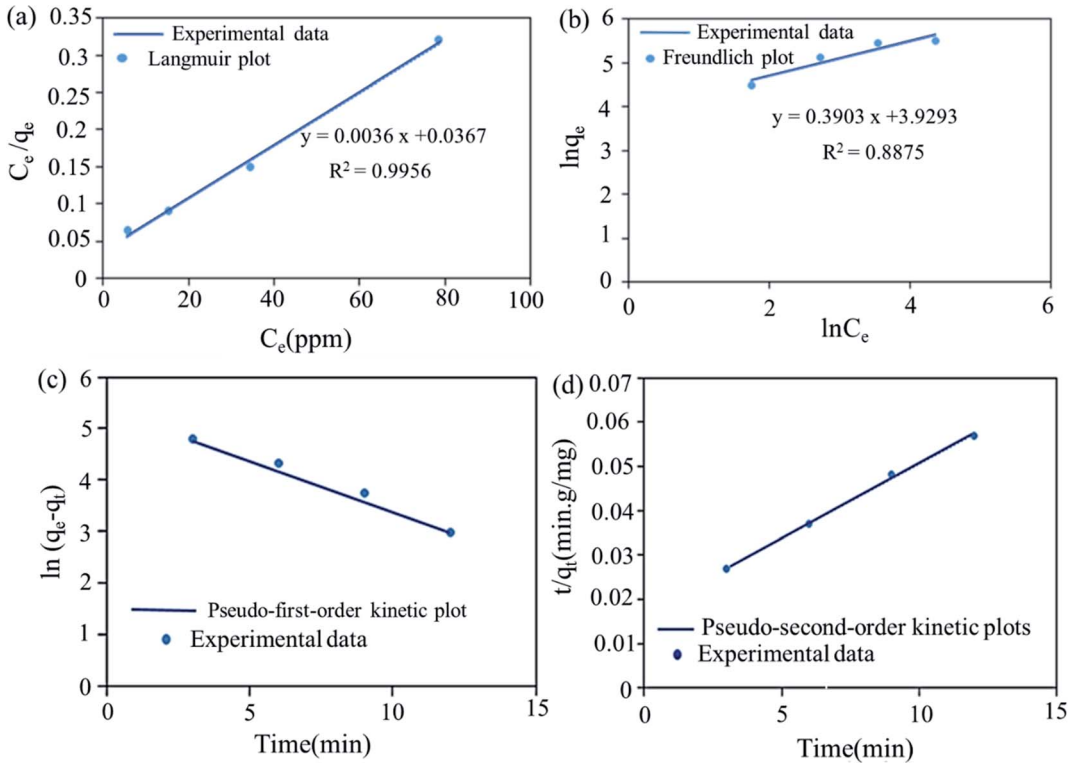

Fig. 10 The corresponding Langmuir plot (a), Freundlich plot (b) for MB adsorption on SMSSO cryogel (c) pseudo-first-order kinetic plot, (d) pseudo-second-order kinetic plots for the adsorption of MB onto SMSSO cryogel.

Open Access Article. Published on 30 May 2022. Downloaded on 12/31/2025 10:40:30 PM.
This article is licensed under a Creative Commons Attribution-NonCommercial 3.0 Unported Licence.

Table 4 Maximum MB adsorption capacity of various adsorbents

Adsorbent	Temp. (°C)	pH	Maximun MB adsorption capacity (mg g^{-1})	Reference
Agar/κ carrageenan hydrogel	35	7	242.3	52
PDA-rGO-kaolin	27	7	39.663	53
Mesoporous iraqi red kaolin clay	29.8	7	240.4	54
ZnS:Ni-NPs-ACATW	r.t	7	21.79	55
GO-CNW nanocomposite	44.85	11	35.3	56
Silica xerogel	40	5	51.967	57
Fava bean peel waste	r.t	5.8	140	58
$Ag_{1.92}Mo_3O_{10}\cdot H_2O$ nanowires	r.t	7	175	26
SMSSO cryogel	60	9	277.77	This work

dye adsorption occurred in monolayer adsorption. The maximum adsorption capacity (q_{max}) of cryogel for MB dye was recorded to be 277.77 mg g^{-1} at 333.15 K.

3.2.7 Kinetics of dye adsorption. The kinetics of MB removal by the synthesized SMSSO ($Ag_2Mo_3O_{10}$@Ag/AgO) cryogel was investigated employing pseudo-first-order (eqn (11)) and pseudo-second-order kinetic equations models (eqn (12))

$$\mathrm{Ln}(q_e - q_t) = \ln q_e - K_1 t \quad (11)$$

The pseudo second order equation is expressed as

$$\frac{t}{q_t} = \frac{1}{K_2 q_e^2} + \frac{t}{q_e} \quad (12)$$

where q_t and q_e (mg g^{-1}) are the amount of adsorbate adsorbed, *i.e.*, adsorption capacities at any time t (min) and equilibrium, respectively. K_1 (min^{-1}) and K_2 (mg g^{-1} min^{-1}) are the pseudo-first-order and pseudo-second-order adsorption rate constants, respectively.

The kinetic parameters and the correlation coefficients (R^2) and the kinetic parameters for pseudo-first-order and pseudo-second-order adsorption are given in Table 3 and Fig. 10c and d. Fig. 10d displays that all experimental data can fit well to the pseudo-second-order model with high correlation coefficients ($R^2 > 0.9986$). This suggests that the present adsorption kinetics followed a pseudo-second-order model. These data infer that the control of adsorption occurs by chemisorption. Moreover, maximum adsorption capacity value of SMSSO cryogel for MB adsorption is compared with other adsorbents and tabulated in Table 4. It can be seen from Table 4 that the synthesized SMSSO cryogel has a higher adsorption capacity compared to some reported adsorbents. Therefore, it may be used as a promising adsorbent for the adsorption of cationic dyes.

3.2.8 Adsorption mechanism. The adsorbent surface has many active sites. Adsorption of MB by the adsorbent involves hydrogen bonds between surface hydroxyl groups with nonbonding electron of N and S atoms. Moreover, complexation can occur between silver nanoparticles surface and nitrogen atoms of MB. Additionally, MB can be absorbed from water through electrostatic interactions of oxygen of $Ag_2Mo_3O_{10}$ nanowires with the positive surface of the dye.[51] The

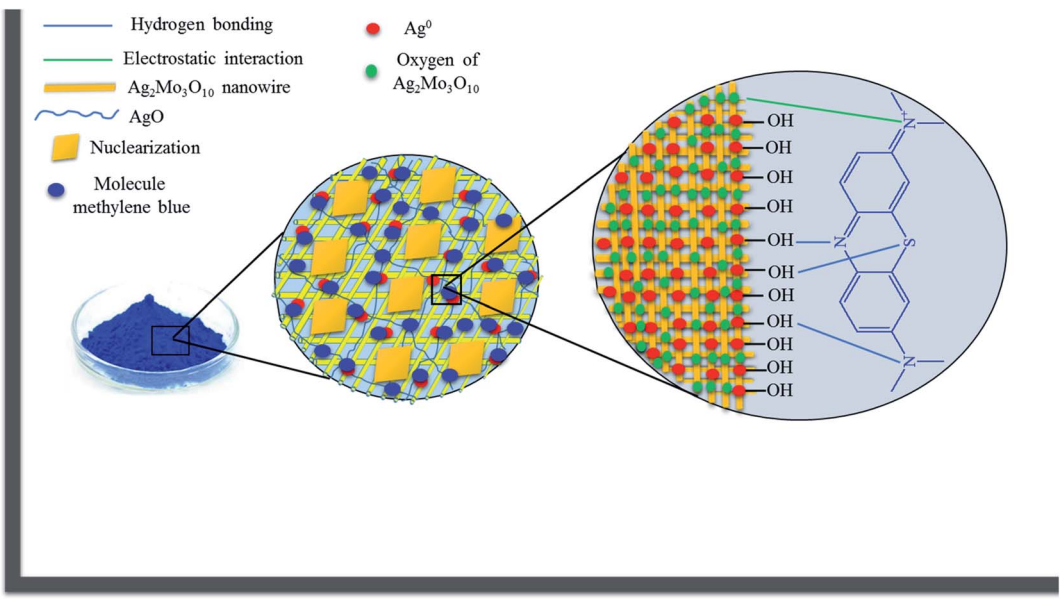

Scheme 2 The proposed mechanism for the adsorption of MB.

© 2022 The Author(s). Published by the Royal Society of Chemistry

Open Access Article. Published on 30 May 2022. Downloaded on 12/31/2025 10:40:30 PM.
This article is licensed under a Creative Commons Attribution-NonCommercial 3.0 Unported Licence.

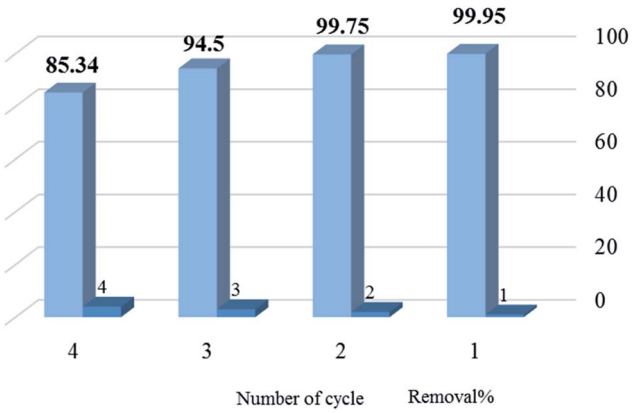

Fig. 11 The removal% of methylene blue by SMSSO at four cycles of operation.

Table 5 Growth inhibition zones for different ratio Ag/Mo of SMSSO cryogel

Different molar ratios Ag/Mo	Zone of inhibition for *E. coli* (mm)	Zone of inhibition for *S. aureus* (mm)
1 : 1	36	32
2 : 1	34	36
3 : 1	41	35
4 : 1	37	34

entanglement of the nanowires and the porous structure of the nanocomposite cryogel could enhance the adsorption capacity by trapping the dye molecules inside the small pores (Scheme 2).

3.2.9. Recycling. The regeneration efficiency of adsorbent is a necessary factor for its practical application. After each adsorption step of 10 mL of methylene blue solution (150 ppm) by 0.01 g of absorbent, the adsorbent was collected by centrifugation, then washed with 25 mL of ethanol (under 1 h continuous stirring), and dried at 80 °C until reused in the next run. The results indicated that the percentage of dye removal in the first three cycles was almost constant and slightly decreased from the fourth cycle (Fig. 11).

3.3 Antibacterial test

The results show that SMSSO cryogels with different ratio Ag/Mo have significant inhibitory effects on the growth of *E. coli* and *S. aureus* bacteria. The diameters of the zones of inhibition for 0.031 gr of SMSSO are tabulated in Table 5.

4 Conclusion

In this research work, for the first time, the cryogel $Ag_2Mo_3O_{10}$@Ag/AgO composite was synthesized through an easy and fast ultrasonic assisted synthesis method. Ultrasonic waves caused the nanowires to grow further and reach a length of several microns. As the ultrasonic treatment continued, nuclei formed and entanglement of very long nanowires led to gel formation. The gel structure was obtained only under sonication in water, in the presence of an excess of silver ions. This process of creating new morphology and gel formation through ultrasonic treatment significantly increased the SMSSO adsorption capacity compared to $Ag_2Mo_3O_{10}$ nanowires. SMSSO was select as an adsorbent to remove MB from an aqueous solution and the maximum adsorption capacity reached about 277.77 mg g^{-1} under the optimal experimental condition. The higher saturation adsorption capacity of SMSSO cryogel nanocomposite, compared to most reported adsorbents, suggested its remarkable efficiency. Pseudo-second order and Langmuir isotherm models suitably describe the kinetics and equilibrium data, respectively.

According to the obtained results, SMSSO exhibited excellent antibacterial properties due to its special morphology, which can increase its ability to treat wastewater. Cryogel of $Ag_2Mo_3O_{10}$@Ag/AgO has a narrow band-gap (~2.8 eV) and could be theoretically suitable photo-catalyst. Consequently, the prepared SMSSO cryogel is expected to be a potential candidate for applications in environmental remediation because of its simple preparation methodology, good antibacterial properties, and excellent dye adsorption capacity.

Conflicts of interest

The authors declare no competing financial interest.

References

1 T. Shindhal, P. Rakholiya, S. Varjani, A. Pandey, H. H. Ngo, W. Guo, H. Y. Ng and M. J. Taherzadeh, *Bioengineered*, 2021, **12**, 70–87.
2 F. M. Alzahrani, N. S. Alsaiari, K. M. Katubi, A. Amari, F. Ben Rebah and M. A. Tahoon, *Polymers*, 2021, **13**, 1742.
3 S. K. Low, M. C. Tan and N. L. Chin, *Ultrason. Sonochem.*, 2018, **48**, 64–70.
4 S. K. Das, M. M. R. Khan, T. Parandhaman, F. Laffir, A. K. Guha, G. Sekaran and A. B. Mandal, *Nanoscale*, 2013, **5**, 5549–5560.
5 S. Lim, J. H. Kim, H. Park, C. Kwak, J. Yang, J. Kim, S. Y. Ryu and J. Lee, *RSC Adv.*, 2021, **11**, 6201–6211.
6 S. Zinatloo-Ajabshir, M. Baladi and M. Salavati-Niasari, *Ultrason. Sonochem.*, 2021, **72**, 105420.
7 H. Liu, J. Zhang, M. Lu, L. Liang, H. Zhang and J. Wei, *Chem. Eng. J.*, 2020, **387**, 124202.
8 S. Hube, M. Eskafi, K. F. Hrafnkelsdóttir, B. Bjarnadóttir, M. Á. Bjarnadóttir, S. Axelsdóttir and B. Wu, *Sci. Total Environ.*, 2020, **710**, 136375.
9 N. H. Ince, *Ultrason. Sonochem.*, 2018, **40**, 97–103.
10 A. Muniyasamy, G. Sivaporul, A. Gopinath, R. Lakshmanan, A. Altaee, A. Achary and P. V. Chellam, *J. Environ. Manage.*, 2020, **265**, 110397.
11 T. Taghipour, G. Karimipour, M. Ghaedi and A. Asfaram, *Ultrason. Sonochem.*, 2018, **41**, 389–396.
12 C. Karthik, N. Swathi and D. Caroline, *J. Environ. Chem. Eng.*, 2020, **8**, 103577.

Open Access Article. Published on 30 May 2022. Downloaded on 12/31/2025 10:40:30 PM. This article is licensed under a Creative Commons Attribution-NonCommercial 3.0 Unported Licence.

13 P. Loganathan, S. Vigneswaran, J. Kandasamy and R. Naidu, *J. Hazard. Mater.*, 2013, **248**, 1–19.
14 O. A. Oyewo, E. E. Elemike, D. C. Onwudiwe and M. S. Onyango, *Int. J. Biol. Macromol.*, 2020, **164**, 2477–2496.
15 A. Azari, R. Nabizadeh, S. Nasseri, A. H. Mahvi and A. R. Mesdaghinia, *Chemosphere*, 2020, **250**, 126238.
16 X. Zhang, Z. Li, S. Lin and P. Théato, *ACS Appl. Mater. Interfaces*, 2020, **12**, 21100–21113.
17 S. Moosavi, C. W. Lai, S. Gan, G. Zamiri, O. Akbarzadeh Pivehzhani and M. R. Johan, *ACS Omega*, 2020, **5**, 20684–20697.
18 Y. Chen, J. Ru, B. Geng, H. Wang, C. Tong, C. Du, S. Wu and H. Liu, *Carbohydr. Polym.*, 2017, **174**, 841–848.
19 S. Shen, Z. Wang, Z. Lin, K. Song, Q. Zhang, F. Meng, L. Gu and W. Zhong, *Adv. Mater.*, 2022, 2110631.
20 Z. Wang, B. Xiao, Z. Lin, Y. Xu, Y. Lin, F. Meng, Q. Zhang, L. Gu, B. Fang and S. Guo, *Angew. Chem.*, 2021, **133**, 23576–23581.
21 D. P. Dutta, A. Singh, A. Ballal and A. K. Tyagi, *Eur. J. Inorg. Chem.*, 2014, **2014**, 5724–5732.
22 S. Vinoth, M. Govindasamy and S.-F. Wang, *Anal. Chim. Acta*, 2022, **1192**, 339355.
23 R. M. Abdelhameed, M. Abu-Elghait and M. El-Shahat, *J. Photochem. Photobiol., A*, 2022, **423**, 113572.
24 Q. Zhang, A. Goldbach, N. Ta and W. Shen, *Appl. Catal., A*, 2021, **623**, 118275.
25 A. Gulpiya, Z. Su and H. Pan, *J. Aust. Ceram. Soc.*, 2021, **57**, 91–96.
26 C. Mondal, J. Pal, K. K. Pal, A. K. Sasmal, M. Ganguly, A. Roy, P. Manna and T. Pal, *Cryst. Growth Des.*, 2014, **14**, 5034–5041.
27 C. Bréchignac, P. Cahuzac, N. Kebaili, A. Lando, A. Masson and M. Schmidt, *J. Chem. Phys.*, 2004, **121**, 9617–9622.
28 E. A. C. Ferreira, N. A. Neto, M. Bomio and F. V. d. Motta, *Ceram. Int.*, 2019, **45**, 11448–11456.
29 C. A. Oliveira, D. P. Volanti, A. E. Nogueira, C. A. Zamperini, C. E. Vergani and E. Longo, *Mater. Des.*, 2017, **115**, 73–81.
30 C. C. De Foggi, R. C. De Oliveira, M. Assis, M. T. Fabbro, V. R. Mastelaro, C. E. Vergani, L. Gracia, J. Andres, E. Longo and A. L. Machado, *Mater. Sci. Eng., Proc. C*, 2020, **111**, 110765.
31 M. Hezarkhani, S. Ustürk, C. Özbilenler and E. Yilmaz, *J. Appl. Polym. Sci.*, 2021, **138**, 50958.
32 A. Nuthanakanti and S. G. Srivatsan, *Nanoscale Adv.*, 2020, **2**, 4161–4171.
33 A. K. Nayak and B. Das, in *Polymeric Gels*, Elsevier, 2018, pp. 3–27.
34 S. Mikhalovsky, I. Savina, M. Dainiak, A. Ivanov and I. Galaev, *Compr. Biotechnol.*, 2011, 11–22.
35 M. Cheraghizade, F. Jamali-Sheini, R. Yousefi, F. Niknia, M. R. Mahmoudian and M. Sookhakian, *Mater. Chem. Phys.*, 2017, **195**, 187–194.
36 H. Gu, X. Chen, F. Chen, X. Zhou and Z. Parsaee, *Ultrason. Sonochem.*, 2018, **41**, 109–119.
37 G. Furtado and A. Medeiros, *J. Clin. Microbiol.*, 1980, **12**, 550–553.
38 S. K. Sen, S. Dutta, M. Khan, M. Manir, S. Dutta, A. Al Mortuza, S. Razia and M. Hakim, *Bionanosci.*, 2019, **9**, 873–882.
39 T. Aditya, J. Jana, R. Sahoo, A. Roy, A. Pal and T. Pal, *Cryst. Growth Des.*, 2017, **17**, 295–307.
40 A. Ziashahabi, M. Prato, Z. Dang, R. Poursalehi and N. Naseri, *Sci. Rep.*, 2019, **9**, 1–12.
41 H. Yang, Y.-y. Ren, T. Wang and C. Wang, *Results Phys.*, 2016, **6**, 299–304.
42 C. He, L. Liu, Z. Fang, J. Li, J. Guo and J. Wei, *Ultrason. Sonochem.*, 2014, **21**, 542–548.
43 K. Zhang, N. Heo, X. Shi and J. H. Park, *J. Phys. Chem. C*, 2013, **117**, 24023–24032.
44 B. Balraj, M. Arulmozhi, C. Siva and R. Krithikadevi, *J. Mater. Sci.: Mater. Electron.*, 2017, **28**, 5906–5912.
45 K. Hakouk, P. Deniard, L. Lajaunie, C. Guillot-Deudon, S. Harel, Z. Wang, B. Huang, H.-J. Koo, M.-H. Whangbo and S. p. Jobic, *Inorg. Chem.*, 2013, **52**, 6440–6449.
46 M. Bujoli-Doeuff, R. m. Dessapt, P. Deniard and S. p. Jobic, *Inorg. Chem.*, 2012, **51**, 142–149.
47 B. Nandi, A. Goswami and M. Purkait, *Appl. Clay Sci.*, 2009, **42**, 583–590.
48 H. Zhang, X. Shi, J. Li, P. Kumar and B. Liu, *Nanomaterials*, 2019, **9**, 1283.
49 F. Mashkoor and A. Nasar, *J. Magn. Magn. Mater.*, 2020, **500**, 166408.
50 I. Tahira, Z. Aslam, A. Abbas, M. Monim-ul-Mehboob, S. Ali and A. Asghar, *Int. J. Biol. Macromol.*, 2019, **136**, 1209–1218.
51 J. Singh and A. Dhaliwal, *J. Polym. Environ.*, 2021, **29**, 71–88.
52 O. Duman, T. G. Polat, C. Ö. Diker and S. Tunç, *Int. J. Biol. Macromol.*, 2020, **160**, 823–835.
53 K. He, G. Zeng, A. Chen, Z. Huang, M. Peng, T. Huang and G. Chen, *Composites, Part B*, 2019, **161**, 141–149.
54 A. H. Jawad and A. S. Abdulhameed, *Surf. Interfaces*, 2020, **18**, 100422.
55 H. Z. Khafri, M. Ghaedi, A. Asfaram and M. Safarpoor, *Ultrason. Sonochem.*, 2017, **38**, 371–380.
56 N. S. Beyranvand, B. Samiey, A. D. Tehrani and K. Soleimani, *J. Chem. Eng. Data*, 2019, **64**, 5558–5570.
57 G. Guzel Kaya, E. Yilmaz and H. Deveci, *J. Chem. Technol. Biotechnol.*, 2019, **94**, 2729–2737.
58 O. S. Bayomie, H. Kandeel, T. Shoeib, H. Yang, N. Youssef and M. M. El-Sayed, *Sci. Rep.*, 2020, **10**, 1–10.

© 2022 The Author(s). Published by the Royal Society of Chemistry